Electromagnetic Pigging System Based on Sandwich Differential Planar Coil

Yupei Yang, Bin Gao, *Senior Member, IEEE*, Dong Liu, *Member, IEEE*, Qiuping Ma, Haoran Li, Wai Lok Woo, *Senior Member, IEEE*, and Gaige Ru

***Abstract*—In-pipeline inspection is an important precontrol method to ensure the safety of oil and gas pipeline transportation. This article proposes an electromagnetic in-pipe detector based on passive resonance-enhanced differential planar coils to detect defects on the inner surface of pipes. Both qualitative and quantitative analyses of pipeline defects and damage are developed. The introduction of passive resonant coils is shown to significantly improve the detection capability of the sensor. This is coupled with the establishment of a theoretical derivation model of the proposed structure. The hardware platform of the laboratory system has been built, and an eddy current internal detector suitable for 8-in-diameter pipes is developed and integrated into the system. Numerical simulations and experimental verifications on flat defects and pipe defects have been undertaken. The obtained results have shown that the real defects have been correctly detected, and the system is effective, reliable, and efficient.**

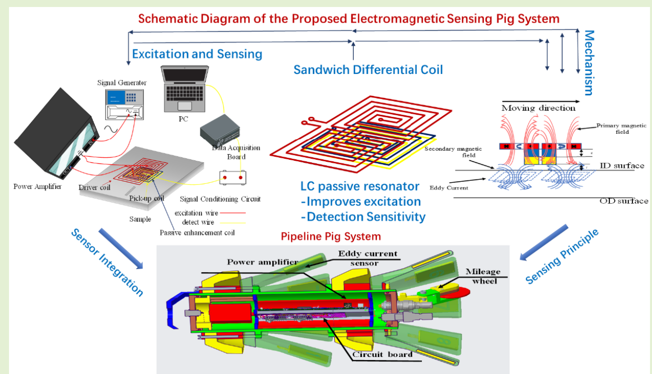

***Index Terms*— Eddy current (EC) testing, in-pipeline inspection, planar coil, resonance enhancement.**

I. Introduction

WITH the continuous improvement in industrialization, huge demands become more prevalent for nondestructive, noninvasive, and noncontact diagnostic mechanisms in maintaining pipeline integrity. There are huge oil and gas pipelines in the world and statistics. Behbahani *et al.* [1] show that the accident rate due to the defects of pipelines is on the rise [2]. Hazards such as cracks, dents, metal loss, or corrosion that occur on the pipe may cause personal injury or death, economic loss, and environmental damage [3]. Thus, correct detection and timely monitoring of pipeline integrity before failure are essential for production and security.

Internal or inline inspection (ILI) technology is recognized as the most effective method for detecting and locating pipeline defects [4], [5], [6], [7]. It moves in the pipeline through nondestructive testing (NDT) methods, such as magnetic flux leakage (MFL), ultrasonic testing (UT), and eddy current (EC), which are equipped with pipeline inspection instruments (PIGs) [8]; potential defective areas were identified after evaluating data [9]. Over the years, in-pipe inspections have been intensified. For example, three-axis high-resolution MFL inspection, liquid ultrasonic crack inspection, electromagnetic acoustic transducer (EMAT) inspection, and remote field EC (RFEC) inspection technologies are proposed to achieve high detection accuracy of pipe defects [10]. In 1965, American Tuboscope Company used the MFL detection method to detect the pipeline [11]. This was the first pipeline inspection tool. MFL PIG is the most frequently used in-line inspection tool. Shenyang University of Technology, Pipetel Company, GE PII Company, and T.D.W Company have already developed PIG and successfully tested it in the gas pipeline. The research team from the Shenyang University of Technology focuses on large-diameter gas pipeline inspection and developed a full range of ultrahigh-definition MFL detectors. They used the finite element method to calculate the influence of magnetic field intensity for defect detection. A high-speed MFL detection experimental platform was

Manuscript received 3 July 2022; revised 1 August 2022; accepted 20 August 2022. Date of current version 30 September 2022. This work was supported in part by the Deyuan and UESTC Joint Research Center; in part by the National Natural Science Foundation of China under Grant 61971093 and Grant 61527803; in part by the International Science and Technology Innovation Cooperation Project of Sichuan Province under Grant 2021YFH0036; and in part by the Science and Technology Department of Sichuan, China, under Grant 2018JY0655 and Grant 2018GZ0047. The associate editor coordinating the review of this article and approving it for publication was Dr. Qammer H. Abbasi. *(Corresponding author: Bin Gao.)*

The authors are with the School of Automation Engineering, University of Electronic Science and Technology of China, Chengdu 611731, China, and also with the Department of Computer and Information Sciences, Northumbria University, Newcastle upon Tyne NE1 7RU, U.K. (e-mail: bin_gao@uestc.edu.cn).

This article has supplementary downloadable material available at https://doi.org/10.1109/JSEN.2022.3201093, provided by the authors.

Digital Object Identifier 10.1109/JSEN.2022.3201093

developed to carry out experimental research on steel pipe defects under different operating speeds and different external magnetic field intensities [12]. Pipetel Company developed the "EXPLORER ILI fleet" for the inspection of 6–36-in-diameter natural gas and liquid pipelines. This tool can move in two directions in the pipeline and enables visual and nondestructive inspection with multipoint data collection. SpirALL MFL (SMFL) is introduced to explore the advantage based on the spiral magnetic leakage structure, while it complements the insufficient of a single-axial magnetic field. The magnetic scan MFL detector developed by GE PII Company is suitable for the pipe diameter range of 76–1422 mm. The high field "speed-stable" magnetizer enables the detection speed of reaching 5 m/s, and 216 Hall effect sensors are integrated for high-resolution detection. EC is useful for crack detection and material thickness measurements. It can adapt to a wider temperature range for operation and its advantages consist of smaller size, lightweight, and relatively lower cost. Rosen Company is dedicated to corrosion detection and heavy-walled pipeline inspection with EC testing. It has developed a pipeline EC internal detector for metal loss, which is combined with a deflection sensor that allows for simultaneous measurement of the inner pipeline contour. Thus, not only corrosion but also deformations can be captured in one run. Many types of EC probes are dedicated to surface defects, especially the application of planar-type probes. Yamada *et al.* [13] presented a dual planar micro coil structure to reduce the noise and improve the strength of the measured signal. It discussed the relationships between resonance frequency and defect detection signal-to-noise ratio. Fava and Ruch [14] calculated the fields produced by planar rectangular spiral coils through the second-order vector potential formulation and impedance plane diagrams with different frequencies, liftoff, and half-space conductivity. Xu and Shida [15] investigated an ECT probe composed of a double uneven step distributing planar coil. The location of cracks on the metal surface can be detected in nonscanning detection mode, while the liftoff should be no more than 1.9 mm. Recently, a planar coil has been used flexibly in various fields. Rosado *et al.* [16] presented a new planar EC probe that can dynamically modify the induced ECs' pattern. It is good for detecting cracks in different orientations. Pasadas *et al.* [17] excited a double-layer planar coil to generate a rotating magnetic field and received it by giant magnetoresistive (GMR) sensor to detect a particular kind of machined cracks with complex geometry. Machado *et al.* [18] designed a new planar ECT array probe to detect unidirectional carbon fiber reinforced polymer (UD CFRP) materials at both high liftoff (up to 3 mm) and velocity (up to 4 m/s). With customized TMR sensors and application-specific integrated circuits (ASICs) for signal processing and interface, Caetano *et al.* [19] disclosed two NDT probes: one for surface defects and the other for buried defects. However, it is mainly used in the laboratory environment at present, and since the liftoff height is low, it is difficult to detect defects in the actual pipeline environment. In this article, a new differential sensing structure based on matching capacitors and passive enhancement coils is proposed. Planar coils have shown to contain the capability of good detection performance in EC

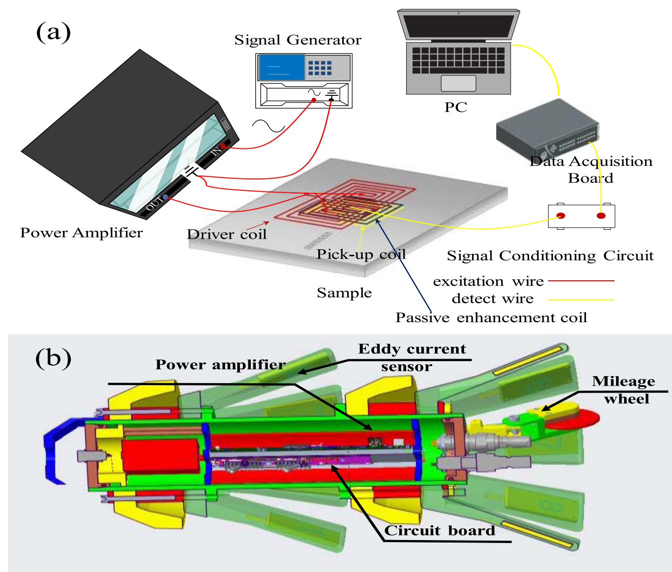

Fig. 1. (a) Testing system frame diagram. (b) Schematic of an intelligent pig.

nondestructive testing. The differential structure can reduce the liftoff impact and the influence of the external environment, such as temperature. The excitation coil adopts rectangular symmetry to form a uniform EC field in the middle of the coil. The multilayer structure of the receiving coil can increase the sensitivity of the detectability. The proposed passive enhancement coil adds a coupling path between the excitation coil, the receiving coil, and the test piece, which enhances the sensitivity of detection. In particular, the capacitance of the receiving coil is adjusted to significantly enlarge the varying amplitude. In particular, we have integrated the proposed probe array with pipeline "PIG." Both simulations and experiments have demonstrated the feasibility of the proposed sensing structure.

The rest of this article is organized as follows. Section II presents the resonance enhancement effect based on the magnetic coupling mutual inductance model and introduces the complete detection system. Section III conducts a finite element simulation with the designed model and presents the experiment results and analysis. Finally, the conclusion is drawn in Section IV.

II. Proposed Methodology

A. Proposed Passive Enhanced Eddy Current Probe and Pipeline Inspection System

The proposed detection system is illustrated in Fig. 1(a) and (b). Fig. 1(a) shows the test system for the detection ability of the probe on the plate under experimental conditions. The Function generator device generates a sine wave of a specific frequency, and the power amplifier is required to increase its output current. The EC coil is excited by the excitation device, which constitutes the ac signal. The data acquisition card collects sensor data, and the PC performs data processing. The EC pipe PIG is shown in Fig. 1(b). The EC pipe pig adopts an integrated petal structure. Also, the EC sensor is encapsulated in the petal, and the

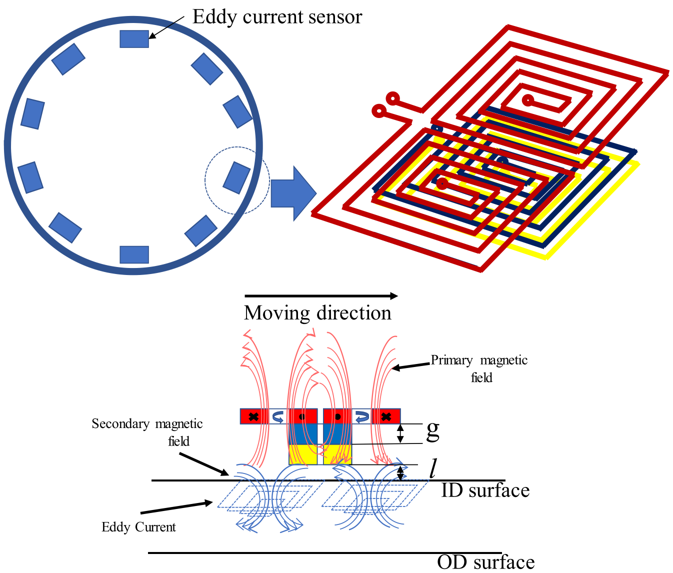

Fig. 2. Magnetic coupling between conductor and proposed probe.

hardware system is placed in the middle cavity of the in-pipe detector.

The structure of the pipe pig is shown in Fig. 1(b). There are 20 measurement channels. The size of the in-pipe detector corresponds to the size of the pipe to be inspected. The hardware system is mainly composed of field programmable gate array (FPGA), microcontroller unit (MCU), analog to digital convert (AD)/digital to analog convert (DA) conversion, power amplifier, and amplitude extraction. The FPGA generates two signals through the DAC: one as the excitation signal and the other as the reference signal. It extracts the amplitude and phase of the signal, and the ADC collects the signal after the extraction. The MCU stores the data sent by the FPGA and communicates with the host computer to complete the data storage and real-time display.

The diagram of the EC sensor structure is shown in Fig. 2. The EC sensor consists of three particular parts: 1) a differential rectangular excitation coil; 2) a four-layer passive enhancement coil with a parallel capacitor in the middle; and 3) a four-layer rectangular receiving coil. The excitation coil adopts a differential rectangular structure, which can not only generate a uniform EC field but also reduce the influence of liftoff and interference. The design of the multilayer receiving coil is built to increase the number of turns of the receiving coil for improving detectability. The passive enhancement coil enhances the coupling between the excitation coil-receiving coil and the test piece to improve the sensitivity of the receiving coil. The capacitance is connected in parallel to the passive enhancement coil to change the coupling. When the position of the excitation coil relative to the test piece has been determined, the capacitance becomes the only factor that affects the change of the inductance of the receiving coil in the sensor. Through experiments, the optimal capacitance value can then be determined.

When the sensor is placed close to the conductor, the EC occurs on the near surface of the conductor. According to Lenz's law, EC in conductors produces opposite magnetic

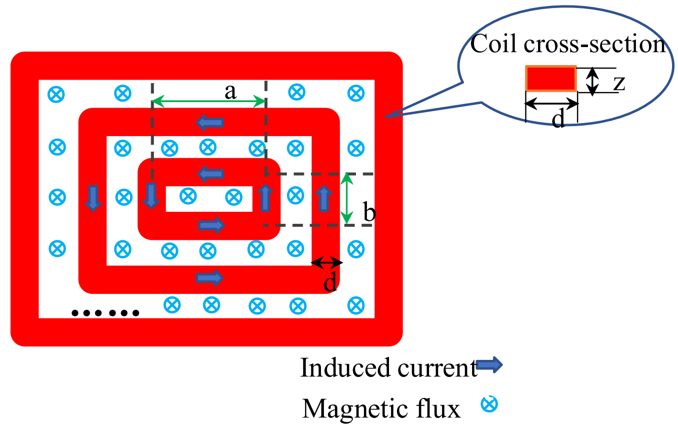

Fig. 3. Coil excitation field.

fields, and it is hindering the change of the original magnetic field (see Fig. 2), where l denotes the liftoff and g is the gap between two layers. A new mutual inductance effect is generated between the excitation coil and the receiving coil.

B. Analysis of the Equivalent Circuit

When a sinusoidal current flows through the excitation coil, an alternating magnetic field is generated. According to Faraday's law, the receiving coil will receive changes in magnetic flux and will generate induced electromotive force (EMF), which can be expressed according to [20] as

$$\varepsilon(t) = -\frac{d}{dt}\iint_S B(x, y, z, t)\cdot dS \tag{1}$$

where z is the thickness of the copper layer, S is the cross section enclosed by the closed wire, B is the magnetic flux on the cross-sectional area, and d is the linewidth and spacing. The induction of a planar coil in a magnetic field is simplified as a superposition of a rectangular coil, which is shown in Fig. 3.

Let B_i be the sum of the magnetic flux density through the area enclosed by loop i. B_i is the time-varying magnetic field generated by the coupling of the primary magnetic field and the secondary magnetic field. The induced voltage on the loops i is determined by B_i [21] According to (2), the induced voltage of the planar coil can be deduced in free space, namely,

$$\varepsilon_i(t) = \frac{j\omega}{zd}\int_{\text{Coil cross-section}}\left(\int_{S_i}\hat{z}B_i\,dS_i\right)d\text{Area} \tag{2}$$

where N is the number of turns of the coil, d is the wire width and spacing, S_i is the area of the loop i, $\omega = 2\pi f$, in which f is the excitation frequency, and Area_i is the coil cross section of the wire. Consider the coil parameters; the voltages can be deduced as follows: define a second-order vector A as it is given by $B = \nabla \times A$. Following Stokes' theorem, (3) is expressed as

$$\varepsilon_i(t) = \frac{j\omega}{zd}\int_{\text{Coil cross-section}}\left(\int_{\Gamma_i}\hat{z}A_i\,dL_i\right)d\text{Area} \tag{3}$$

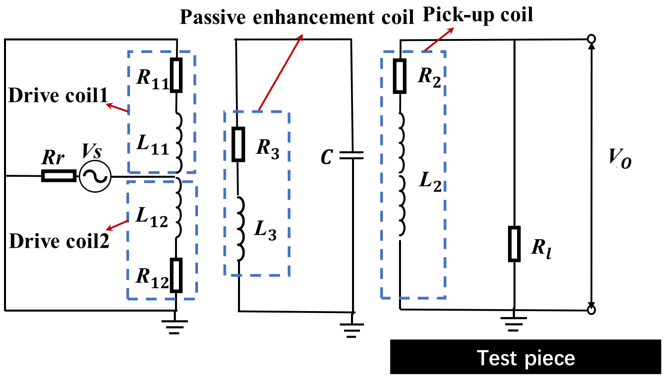

Fig. 4. Schematic of the probe circuit.

where Γ_i is the circumference of loop i, which is determined by a, b, and d. n is the number of turns of the pickup coil. A_i is determined by the size and shape of the probe, and the gap g between the detecting coil and the excitation, respectively. From (3), it is obvious that the induced voltages relate to the parameters of coil and excitation conditions [22]. To simplify the process, we employ circuit schematics for interpretation. The equivalent circuit diagram of the system is shown in Fig. 4. To ensure the same magnetic field, the excitation coil requires applying the same voltage, where it is placed parallel at both ends of the power supply [22], [23], [24], [25]. According to the Biot–Savart law, the magnetic flux relationship between the excitation and reception coils can be calculated, and the mutual inductance M can be solved by Neuman's formula [26] as

$$M=\frac{2\mu_0\sqrt{a\cdot c}}{\alpha}\cdot\left[\left(1-\frac{a^2}{2}\right)K(\alpha)-E(\alpha)\right] \tag{4}$$

$$\alpha=2\sqrt{a\cdot\frac{c}{\left[(a+c)^2+g^2\right]}} \tag{5}$$

where $2a$ and $2c$ are the diameters of two coils and g is the gap between two coils and

$$K(\alpha)=\int_0^{\frac{\pi}{2}}\frac{d\theta}{\sqrt{1-\alpha^2\sin^2\theta}} \tag{6}$$

and

$$E(\alpha)=\int_0^{\frac{\pi}{2}}\sqrt{1-\alpha^2\sin^2\theta}\,d\theta \tag{7}$$

are the first and second complete elliptic integrals, respectively. θ is the angle between the coils.

According to (7), the mutual inductance is related to the parameters of the coil, and the gap g between the excitation and receiving coils plays an important role in the mutual inductance. That is to say, although the differential structure can suppress the effect of the primary magnetic field, the mutual inductance effect can cause changes in the impedance of the detection coil, which can affect the detection results. Selecting the correct coupling spacing can improve detection liftoff and maintain sensitivity.

V_s is the input voltage, R_r is the internal resistance of the excitation device, R_{11}, R_{12} and L_{11}, L_{12} are the internal resistance and inductance of the two excitation coils, respectively, and R_2 and L_2 constitute the detection coil. C is the capacitor connected in parallel to the enhancement coil, and V_o is the output voltage. Thus, these data analyzed the differential coupled circuit with and without a passive enhancement coil. For the convenience of analysis, the circuit diagram can be simplified into Fig. 5(a) and (b), respectively [23], [24].

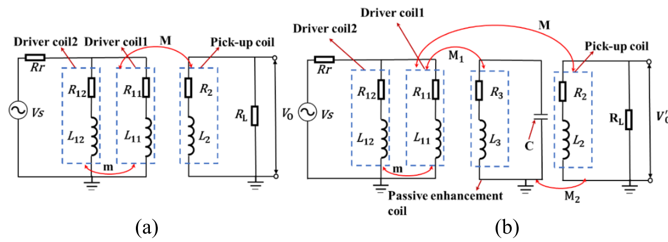

Fig. 5. Equivalent circuit of the probe (a) without passive enhancement coil and (b) with passive enhancement coil.

According to Kirchhoff's law, the voltage depicted in Fig. 5(a) can be calculated as

$$\varepsilon_1(\omega)=-j\omega I_2 M \tag{8}$$

$$\varepsilon_2(\omega)=-j\omega(I_{11}-I_{12})M \tag{9}$$

$$Z_{11}I_{11}+j\omega I_{12}m+(I_{11}+I_{12})\times R_r-j\omega I_2 M=V_s \tag{10}$$

$$Z_2 I_2-j\omega(I_{11}-I_{12})M=0 \tag{11}$$

$$Z_{11}I_{11}+j\omega I_{12}m=Z_{12}I_{12}+j\omega I_{11}. \tag{12}$$

The optimized coil structure is shown in Fig. 5(b), and the voltage depicted in Fig. 5(b) can be calculated as

$$\varepsilon_1(\omega)=-j\omega I_2 M \tag{13}$$

$$\varepsilon_2(\omega)=-j\omega(I_{11}-I_{12})M \tag{14}$$

$$Z_{11}I_{11}+j\omega I_{12}m+(I_{11}+I_{12})R_r-j\omega I_2 M-j\omega I_3 M_1=V_s \tag{15}$$

$$Z_2 I_2-j\omega(I_{11}-I_{12})M-j\omega I_3 M_2=0 \tag{16}$$

$$Z_{11}I_{11}+j\omega I_{12}m=Z_{12}I_{12}+j\omega I_{11}m \tag{17}$$

$$Z_3 I_3-j\omega(I_{11}-I_{12})M_1-j\omega I_2 M_2=0. \tag{18}$$

$Z_{11}=R_{11}+j\omega L_{11}$, $Z_{12}=R_{12}+j\omega L_{12}$, $Z_2=R_2+j\omega L_2$, $Z_3=(R_3^2+(j\omega L_3-(1/j\omega C))^2)^{1/2}$ which represents the impedance of the driver coil, the pickup coil, and the passive enhancement coil. I_{11}, I_{12}, I_2, and I_3 are the current flowing through the excitation coils, the detection coil, and the passive enhancement coil, respectively. The term M is the mutual inductance between the driver coil and the pickup coil. M is the mutual inductance between two driver coils. M_1 is the mutual inductance between the driver coil and the passive enhancement coil, and M_2 is the mutual inductance between the passive enhancement coil and the pickup coil. Therefore, the output voltage V_O can be solved as

$$\begin{aligned}V_O&=I_2R_L\\&=[j\omega M V_S(Z_{12}-Z_{11})R_L]\div[Z_2Z_{11}Z_{12}\\&\quad+(Z_{12}+Z_{11}-2j\omega m)R_rZ_2\ (19)\\&\quad+(Z_{12}-Z_{11}+Z_2)\omega^2M^2]\end{aligned} \tag{19}$$

$$V_0' = [\omega^2 M_1 M_2 V_S (Z_{12} - Z_{11}) R_L] \div [Z_3 Z_{11} Z_{12} Z_2 + (Z_{12} + Z_{11} - 2j\omega m) R_r Z_3 Z_2 + (Z_{12} - Z_{11} + Z_3) Z_2 \omega^2 M_1^2] \tag{20}$$

$$V_1 = V_0 + V_0'. \tag{21}$$

Fig. 5 shows the place of the passive enhancement coil between the excitation coil and the receiving coil. This can increase the coupling between the excitation coil and the receiving coil, thereby improving the detection sensitivity.

From (22), when changing the capacitance of the receiving coil in parallel, the impedance of the receiving coil can be changed to affect the sensitivity of the detection. As long as the probe is placed close to the conductor, the mutual inductance M will be affected by the mutual inductance between the specimen and the coil. $M' = M + \Delta M$; this represents the mutual inductance affected by the sample and the parameters of coils. $Z' = Z + \Delta Z$; it is defined as a transfer impedance that is influenced by the condition of the sample. If the sample has defects near the surface, the bias of impendence between two driver coils will lead the V_O over zero.

III. Experimental Setup

A. Numerical Simulation

To verify the detection capability of the probe structure, finite element simulation models are established in COMSOL Multiphysics software. This study mainly directs at the sensitivity of the new probe for detectability under high liftoff impact. The 3-D model in the software is used to construct the proposed probe. The computational complexity of the model is reduced by using meshes with different densities for different regions. Especially, the frequency-domain analysis is used to analyze models. All the flaw detection simulation experiments on flat plates and pipes are implemented under the magnetic field module.

The schematic of the simulation model view is shown in Fig. 6(a). Specifically, the spiral coil is made of copper, and the simulated size model configuration is shown in the Supplementary Material. The wire diameter of the excitation coil is 0.254 mm, and the wire diameters of the passive enhancement coil and the receiving coil are both 0.0889 mm. In these simulation experiments, the voltage is set to 10 V, while the excitation frequency is set to 1 MHz. The results of defect detection are obtained from the inductive voltage of the detection coil. In addition, the EC distribution diagram is shown in Fig. 6(b). The proposed structure forms a symmetrical EC field. In particular, the uniform field distribution will be generated, which has a positive influence on the detection. It is expected to obtain maximum disturbance of EC once defects exist. Thus, the uniform EC field has obvious advantages in defect detection. The symmetrical excitation of the plane rectangular coil is used to generate a more uniform EC field on the pipe surface to improve the detection sensitivity.

The distribution of EC in the nondefective area of the specimen is studied. The different defect characteristics in ferromagnetic specimens and pipe specimens were verified.

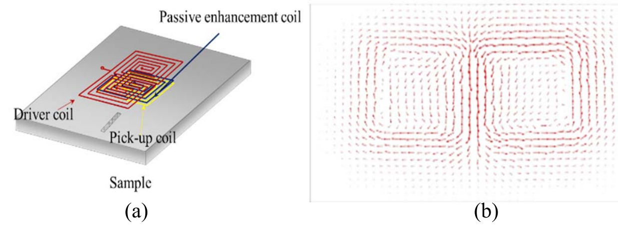

Fig. 6. (a) Model diagram of the probe. (b) Finite element simulation of EC field of the probe.

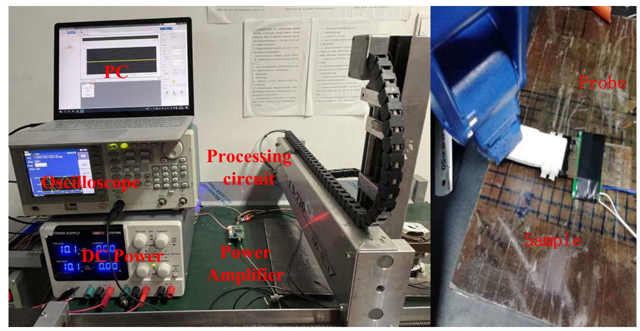

Fig. 7. Experiment platform and inspection system.

In the experiment, 80# steel is ferromagnetic steel. The specific simulation details can be found in the Supplementary Material.

B. Experimental Validation

1) Experimental Platform and Inspection System: Fig. 7 illustrates the experimental verification for artificial defects detection and shows the detection of flat plate defects in a laboratory environment. The probe is connected by three separate layers of PCB. A specimen is produced to match the simulation study, while defects are made with different widths, heights, and shapes, as shown in Table I. The excitation mode is composed of a signal generator and power amplifier. The detection mode conducts the ADA4870 instrument amplifier to enhance the signal, and AD8302 is used to extract the induced voltage. After passing the low-pass filter, the NI-6226 data acquisition card is used for data acquisition. In the experiment, it is found that, due to different material parameters and probe sizes, the results in the simulation can deviate slightly from the results in the experiment. Also, the experiment is affected by the speed effect, which leads to the asymmetry of signal acquisition. Similar to the simulation, the detection direction is divided into A-, B-, C-, and D-axes. The probe is clamped by the XYZ table, and the specimen is scanned in three directions (Fig. 8). The detection speed is 20 mm/s, and the liftoff value is controlled at certain heights of 5, 7, 9, and 11 mm, respectively. Fig. 9 shows the structure of the proposed pipeline pigging system. It is implemented using FPGA based on direct digital frequency synthesis technology to generate a sine wave with adjustable frequency. The generated signal excites the excitation coil through the power amplifier ADA4870, then receives the signal from the EC sensor through an analog-to-digital converter, and generates a file record. The entire control process is controlled by STM32.

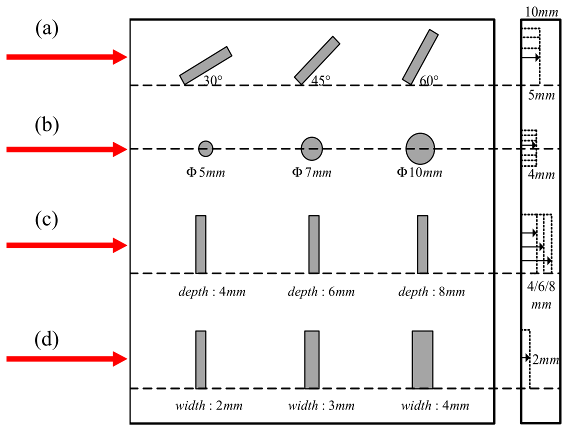

Fig. 8. Simulation of multiple defects under different liftoff conditions.

TABLE I
PARAMETERS OF SIMULATION

Type of defect	Width change			Diameter change			Height change			Angle change		
	a1	b1	c1	a2	b2	c2	a3	b3	c3	a4	b4	c4
Length(mm)	10						10			10		
Width(mm)	4	3	2				2			2		
Height(mm)	4			4			8	6	4	4		
Angle(Compared to Y axis)	90°			90°			90°			60°	45°	30°
Diameter(mm)				10	7	5						

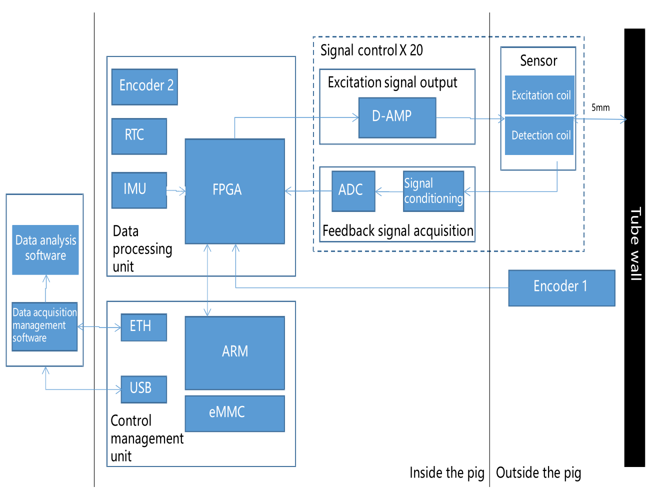

Fig. 9. Pipeline smart pigging system.

The actual frequency used by the sensor is 1 MHz. For determining this frequency, we simulate a detection situation of the sensor on the test piece by simulation of COMSOL Multiphysics software. The simulation is basically in line with the actual situation where individual sensors are shown to work simultaneously. All sensors work at the same time in order to comprehensively cover the pipeline. The test sample is 80# steel. Fig. 10(a) and (b) shows the use of the internal detector to detect the internal defects of the whole pipe in a laboratory environment. The EC sensor array is packaged in the blade of the pigging, while the hardware is placed in the cavity in the middle of the pigging. Fig. 11 shows the structure of the proposed EC sensor.

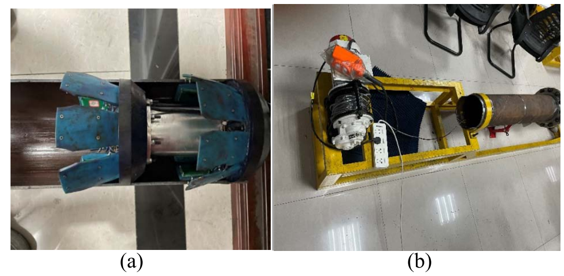

Fig. 10. (a) Smart pigging. (b) Detection system for pipeline defects.

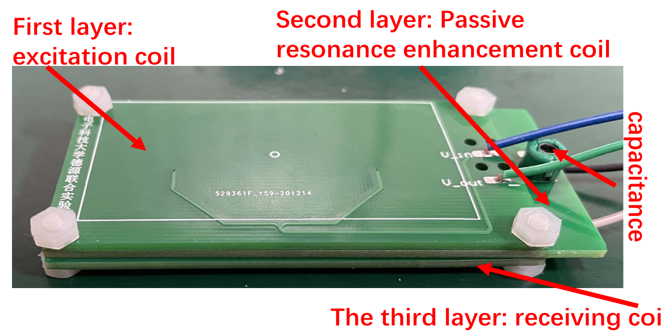

Fig. 11. Physical image of the sensor.

A specimen is produced to match the simulation study, while defects are made with different widths, heights, and shapes, as shown in Fig. 8. Fig. 12 shows natural corrosion pits and cracks. The depth of the pit is approximate 3 mm, and the depth of the crack is around 1 mm. Fig. 13 shows the artificial defects and welds inside the pipeline. Scanning is divided into three directions: A, B, C, and the sizes of defects $(a-h)$ are $20\times 40\times 3$, $20\times 3\times 3$, $r=2$, $10\times 2\times 2$, $20\times 10\times 2$, $3\times 10\times 1$, $80\times 40\times 5$, and $20\times 40\times 5$ mm^3, respectively. The pipe material is 80# steel.

C. Experimental Result Analysis

For EC testing, in order to quantitatively evaluate the detection sensitivity of the system, parameter S is determined, which is expressed as follows [27]:

$$S=\frac{|\text{Max}\,(V_{\text{defect}}-V_{\text{normal}})|}{\text{Max}\,(V_{\text{normal}})} \tag{22}$$

where S is the sensitivity of detection in the corresponding place, V_{defect} indicates the voltage value of coil probes when there is a defect, and V_{normal} means no defect.

Fig. 8 shows the scan process by controlling the XYZ workbench under the same experimental conditions; different defects of the sensor without resonance enhancement and the sensor with resonance enhancement were tested at the same time. Fig. 14 summarizes the detection results of the optimized sensor and the nonoptimized sensor of the angular defect under different peeling values. Table II shows the S value of the

TABLE II
PLATE DEFECT DETECTION RESULTS

Parameters of defect	5mm		7mm		9mm		11mm	
	ΔV(v)	Sensitivity	ΔV(v)	Sensitivity	ΔV(v)	Sensitivity	ΔV(v)	Sensitivity
Angle of defect(mm) 30° 45° 60°	3.7,3.0,2.8	18.6,14.0,13.1	1.9,1.4,0.7	9.3,6.9,3.7	0.8,0.6,0.4	4.0,1.8,1.0	0.6,0.1,0.06	3.1,0.6,0.3
Diameter of circular defect 5 7 10	3.3,2.2,0.9	16.5,11.2,4.6	2.6,1.04,0.32	13,5.2,1.6	1.8,0.1,0.2	8.8,2.0,0.2	0.8,0.05,0.2	4,0.3,0.8
Height of defect(mm) 4 6 8	6.6,6.2,3.6	33.1,30.9,18.1	3.7,3.4,1.8	18.4,17,9.1	1.7,1.6,1.5	8.7,7.9,7.3	1.4,1.2,1.1	6.9,6.0,5.7
Width of defect(mm) 2 3 4	5.4,4.9,3.8	27.1,24.7,19.5	2.5,2.4,1.9	12.4,11.9,9.6	1.0,0.8,0.6	4.9,3.8,3.0	0.9,0.5,0.4	4.7,2.3,1.8
Natural corrosion cracking	0.7	6.3	0.4	4.1	0.1			0.9
Natural corrosion pit 1 2 3	2.2,1.8,1.5	21.8,17.5,14.9	1.1,1.1,0.6	10.8,11.4,5.9	0.6,0.5,0.2			5.5,4.9,2.3

Fig. 12. Natural corrosion pits and natural corrosion cracks.

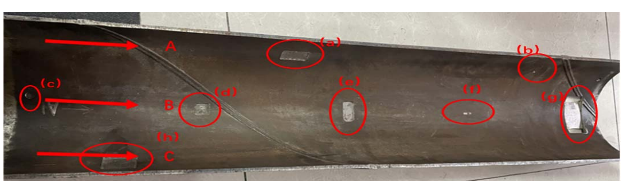

Fig. 13. (a)–(c) Induced voltage of pipeline detection axes *A*, *B*, and *C* with resonance enhancement.

detection results of different defects using optimized sensors and unoptimized sensors. $\Delta V1(v)$ is the voltage change of the optimized sensor. $\Delta V2(mv)$ is the voltage change of the unoptimized sensor. From Fig. 14(a) and (b), it can be seen that there exist voltage fluctuations when scanning defects, and the voltage change of the optimized sensor is more noticeable than that of the unoptimized sensor. In addition, when there is an unoptimized sensor lifted by 7 mm, it becomes difficult to detect the defects. On the other hand, the optimized sensor is still able to detect defects even if it is raised by 11 mm in the same hardware configuration. Through the sensitivity comparison of Table II, the two sensors are more sensitive to depth defects. As the liftoff increases, the defect detection ability becomes weaker. In the case of 5- and 7-mm liftoffs, the two sensors are more sensitive to the same defect. In terms of sensitivity comparison, the sensitivity of the optimized sensor has reached an average of 634% improvement.

TABLE III
PIPELINE DEFECT DETECTION RESULTS

defect	a	b	c	d	e	f	g	h
ΔV(mv)	95.4	192	172.6	103	200.7	130.2	860.8	221
Sensitivity	0.51	1	0.52	0.29	0.58	0.39	11.73	1.28

Enhancement of sensor detection capability by passive resonance effect was tested at the same time. Due to the relatively high liftoff value, the coil without resonance enhancement cannot detect defects in the existing hardware system. Fig. 15(a)–(c) shows the sensor signal with resonance enhancement. The specific detection and analysis results are listed in Table III. The analysis shows that the unoptimized sensor has low sensitivity when the liftoff value is 1 cm, and it cannot detect defects efficiently enough. The optimized sensor, on the other hand, has better detection sensitivity. Therefore, the coil with resonance enhancement has a stronger detection ability than the coil without resonance enhancement, and several defective samples were tested to verify the effectiveness of resonance enhancement.

D. Comparison Verification of Pipeline Defects

In order to verify the advantages of the proposed probe, we compared the traditional U-shaped yoke probe and planar EC probe structures. The U-shaped yoke probe was designed,

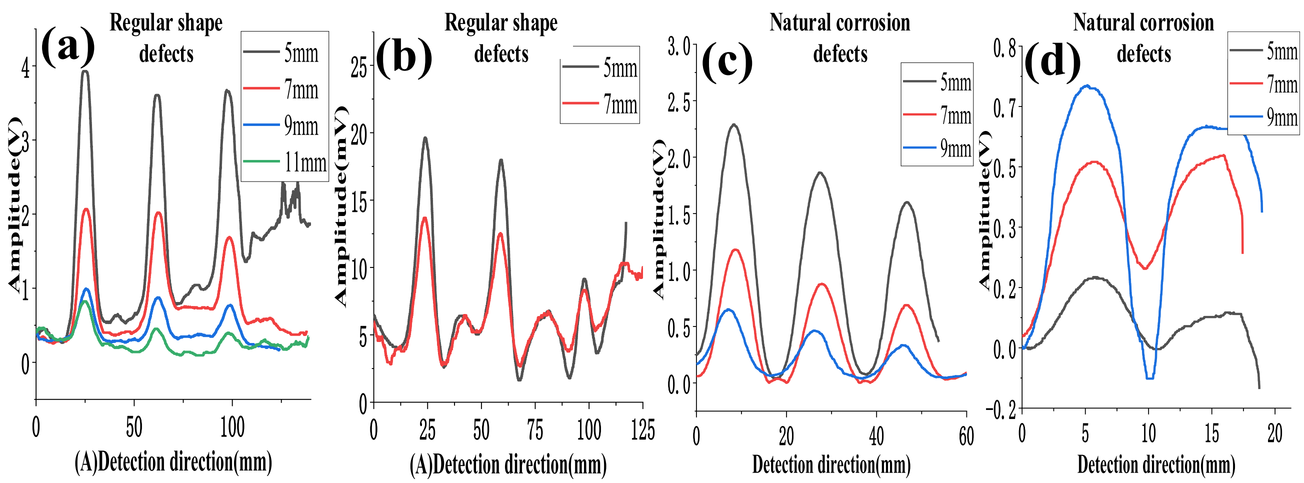

Fig. 14. (a) and (b) Artificial defects detection axis *A* with resonance without resonance enhancement. (c) and (d) Corrosion pit and crack defect signal diagram.

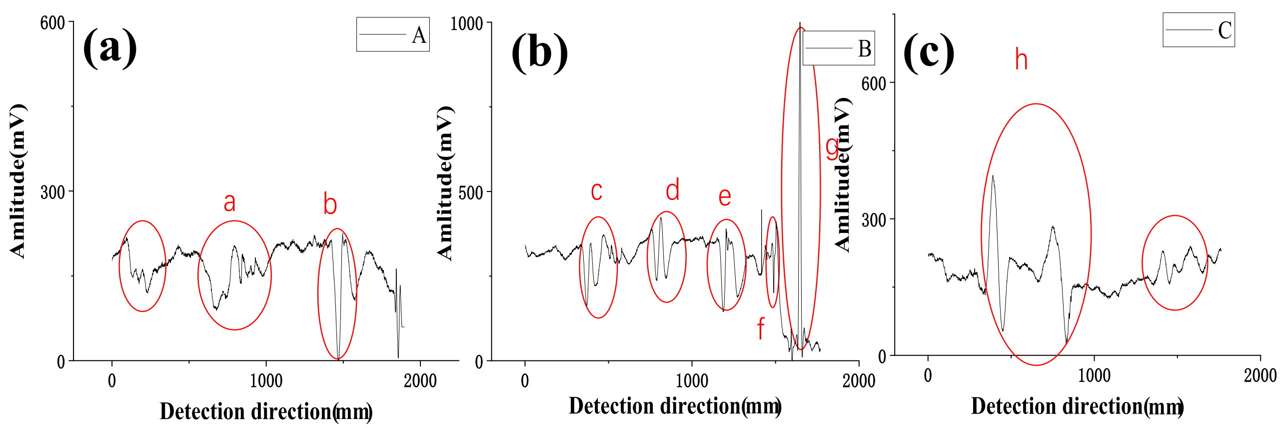

Fig. 15. Artificial defects and welds inside the pipeline. (a) Detection results along the A axis. (b) Detection results along the B axis. (c) Detection results along the C axis.

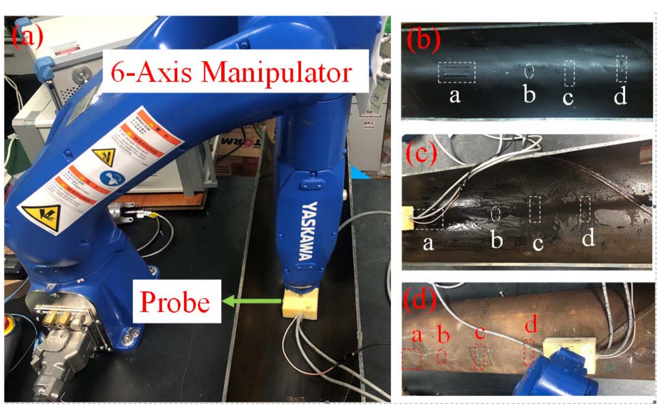

Fig. 16. Schematic of the pipe inspection testing system. (a) Scanning process. (b) Defects inside the pipeline. (c) Internal condition of the pipeline. (d) Defects outside the pipeline.

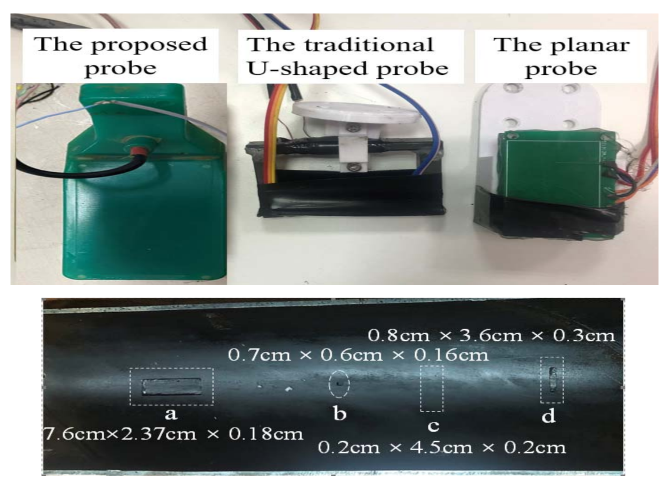

Fig. 17. (a) Probes' structure. (b) Pipeline defect distribution.

referring to ACFM probes, as reported in [28]. The planar probe was designed, referring to EC probes, as reported in [29]. The specific experimental setup is shown in Fig. 16. Fig. 16 compares the detection effects of different internal detection methods on the internal defects of the pipeline. Due to the size and volume of the probes, they cannot be packaged and integrated into the current internal detector. Therefore, a robotic arm is used to support different probes to detect pipeline defects with the same parameters. Fig. 16(c) shows that the probe is controlled by the six-axis manipulator to scan the pipeline. The scanning speed is 20 mm/s,

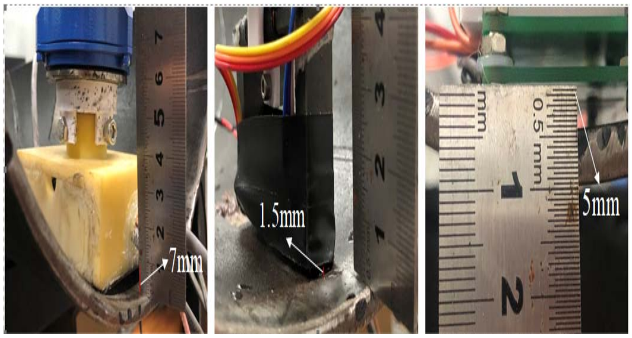

Fig. 18. Liftoff of different probes.

TABLE IV
COMPARISON OF THE PROBES

<table>
<tr><td>The probes structure</td><td colspan="2">The proposed probe</td><td>Traditional U-shaped yoke probe</td><td>Chen (2021)</td></tr>
<tr><td>Sensor</td><td colspan="2">Coil</td><td>TMR</td><td>Coil</td></tr>
<tr><td>Excitation method</td><td colspan="2">Coil</td><td>Yoke</td><td>Coil</td></tr>
<tr><td>Excitation frequency</td><td colspan="2">1MHz</td><td>4kHz</td><td>2MHz</td></tr>
<tr><td>Turns</td><td colspan="2">20</td><td>150</td><td>20</td></tr>
<tr><td>Length (mm)</td><td colspan="2">48</td><td>67</td><td>48</td></tr>
<tr><td>Width (mm)</td><td colspan="2">30</td><td>12</td><td>30</td></tr>
<tr><td>Height (mm)</td><td colspan="2">11</td><td>44</td><td>10</td></tr>
<tr><td rowspan="2">Type and approximate size of Pipe Defects (mm)</td><td>The axial surface defect (a)</td><td>The square surface defect (b)</td><td>The circumferential sub-surface defect (c)</td><td>The circumferential surface defect (d)</td></tr>
<tr><td>76×23.7×1.8</td><td>7×6×1.6</td><td>2×45×2</td><td>8×36×3</td></tr>
</table>

and the scanning distance is 600 mm. Fig. 16(d) shows the experimental state of butter. In order to prevent clogging of the inner detector in the laboratory environment, butter is applied inside the pipe to increase the passage of the inner detector. Fig. 16(d) shows the inspection on the outside of the pipeline. Fig. 16(b)–(d) shows four defects under different viewing angles, respectively. The parameters of different sensors are shown in Table IV. The metrics of different probes are listed in Table IV. The experiment is divided into the comparison of the detectability and sensitivity of the probe to different pipeline defects. By comparing different sensors, it is verified that the proposed sensor can achieve better detection capability at higher liftoff. This section actually discusses the impaction with different liftoff distances. Fig. 17(a) shows the compared sensor structure. Fig.17(b) shows the overall defect distribution. Fig. 18 shows the liftoff of the test experiments.

By comparing Fig. 19(a)–(c), it can be observed that defects #a and #d on the inner side of the pipeline can be identified by all three probes. Defect #b can be detected by the proposed probe and planar probe through feature analysis. The traditional U-shaped probe cannot identify defect #b. The proposed probe can clearly identify the subsurface defect #c, while the planar probe fails to detect defect #b. The test results show that the proposed probe has high

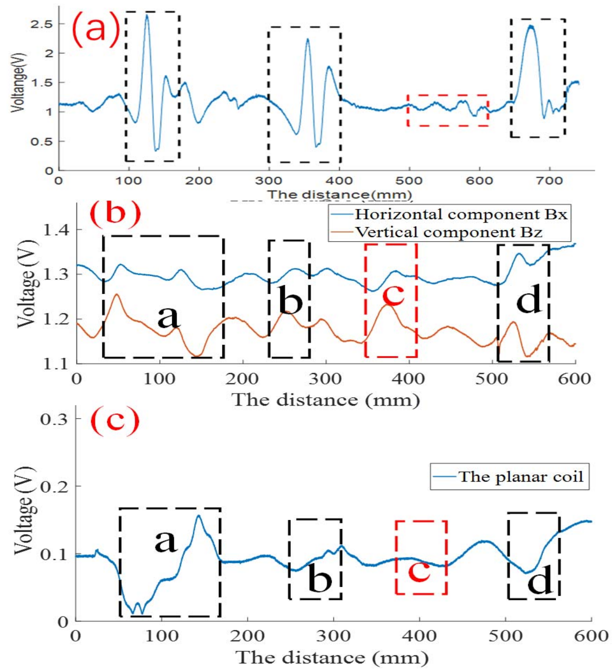

Fig. 19. Test results of different types of probes inside the pipeline. (a) Proposed probe. (b) Traditional U-shaped yoke probe. (c) Planar probe.

TABLE V
COMPARISON RESULTS

Probe type for pipe inspection	Proposed probe				Traditional U-shaped yoke probe				Chen (2021)			
Inner pipeline defect inspection	a	b	c	d	a	b	c	d	a	b	c	d
Sensitivity (Bz or Pcb coil)	1.7	1.3	0.2	1.5	1.1	0.04 0.3	0.2 0.9	1.0 1.1	1.9	0.51	0.03	0.64
Efficacy (Detectability)	D4/4				3/4				3/4			
Precise	√	√	√	√	√	×	√	√	√	√	×	√
Bz SNR (dB)	4.6	2.3	-14.0	3.5	6.9	-10	-0.9	0.83	5.6	-5.8	-30	-3.9

Note: √ and × indicates detected and not detected respectively

$$S=\left|\frac{Max(V_{Defect}-V_{(Defect-free)})}{V_{(Defect-free)}}\right| \quad SNR=20\,log_{10}\left(\frac{V_{aD}}{V_{aN}}\right)[dB]$$

sensitivity and SNR in detecting small defects and subsurface defects.

The evaluation is conducted by normalizing the experimental results due to the balance of different scale ranges of the different probes, as shown in (23), and then solving the corresponding sensitivity. The results are shown in Table V

$$\text{Normalization}=\frac{x-\min(x)}{\max(x)-\min(x)}. \tag{23}$$

IV. CONCLUSION

This article has presented a design of an EC smart pig based on a sandwiched symmetrical differential planar probe. It is composed of an excitation coil, a passive resonance enhancement coil, and a detection coil. By comparing the coil without resonance enhancement and the coil with resonance enhancement, under the liftoff values of 5 and 7 mm, the sensitivity has reached an average of 634%, and the liftoff impact has been significantly resolved. In addition, the detection of flat plate and pipeline defects about 1-cm liftoff value has been realized. It has successfully detected surface microdefects and corrosion defects with high sensitivity. Future work will focus on improving detection sensitivity, defect quantification, and the detection of both internal and external defects in the pipeline.

References

[1] H. Lu, S. Behbahani, M. Azimi, J. C. Matthews, S. Han, and T. Iseley, "Trenchless construction technologies for oil and gas pipelines: State-of-the-art review," *J. Construction Eng. Manage.*, vol. 146, no. 6, Jun. 2020, Art. no. 03120001.

[2] K. Zakikhani, F. Nasiri, and T. Zayed, "A review of failure prediction models for oil and gas pipelines," *J. Pipeline Syst. Eng. Pract.*, vol. 11, no. 1, Feb. 2020, Art. no. 03119001.

[3] M. Coramik and Y. Ege, "Discontinuity inspection in pipelines: A comparison review," *Measurement*, vol. 111, pp. 359–373, Dec. 2017.

[4] G. Tian, B. Gao, Y. Gao, P. Wang, H. Wang, and Y. Shi, "Review of railway rail defect non-destructive testing and monitoring," *Chin. J. Sci. Instrum.*, vol. 37, no. 8, 2016.

[5] R. Bickerstaff, M. Vaughn, G. Stoker, M. Hassard, and M. Garrett, "Review of sensor technologies for in-line inspection of natural gas pipelines," Sandia Nat. Laboratories, Albuquerque, NM, USA, Tech. Rep., 2002.

[6] M. Z. A. Rashid *et al.*, "Modeling of the in-pipe inspection robot: A comprehensive review," *Ocean Eng.*, vol. 203, May 2020, Art. no. 107206.

[7] H. A. Kishawy and H. A. Gabbar, "Review of pipeline integrity management practices," *Int. J. Press. Vessels Pip.*, vol. 87, no. 7, pp. 373–380, Jul. 2010.

[8] H. Song *et al.*, "Comparative analysis of in-line inspection equipments and technologies," in *Proc. IOP Conf. Mater. Sci. Eng.*, vol. 382, no. 3. Bristol, U.K.: IOP, 2018, Art. no. 032021.

[9] Y. N. Duan, Z. J. Han, G. Z. Li, and H. Tian, "Research on key technologies of the cableless pipeline robot," in *Advanced Materials Research*, vol. 591. Bäch, Switzerland: Trans Tech, 2012, pp. 1221–1224.

[10] Q. Feng, R. Li, B. Nie, S. Liu, L. Zhao, and H. Zhang, "Literature review: Theory and application of in-line inspection technologies for oil and gas pipeline girth weld defection," *Sensors*, vol. 17, no. 12, p. 50, Dec. 2016.

[11] M. P. Papaelias, M. C. Lugg, C. Roberts, and C. L. Davis, "High-speed inspection of rails using ACFM techniques," *NDT E Int.*, vol. 42, no. 4, pp. 328–335, 2009.

[12] L. Yang, T. Guo, S. Gao, and B. Liu, "Feature analysis on magnetic flux leakage detection signals for special parts of oil and gas pipelines," *J. Shenyang Univ. Technol.*, vol. 39, no. 1, pp. 43–47, 2017.

[13] S. Yamada, M. Katou, M. Iwahara, and F. P. Dawson, "Eddy current testing probe composed of planar coils," *IEEE Trans. Magn.*, vol. 31, no. 6, pp. 3185–3187, Nov. 1995.

[14] J. O. Fava and M. C. Ruch, "Calculation and simulation of impedance diagrams of planar rectangular spiral coils for eddy current testing," *NDT E Int.*, vol. 39, no. 5, pp. 414–424, Jul. 2006.

[15] P. Xu and K. Shida, "Eddy current sensor with a novel probe for crack position detection," in *Proc. IEEE Int. Conf. Ind. Technol.*, Apr. 2008, pp. 1–6.

[16] L. S. Rosado, T. G. Santos, P. M. Ramos, P. Vilaça, and M. Piedade, "A new dual driver planar eddy current probe with dynamically controlled induction pattern," *NDT E Int.*, vol. 70, pp. 29–37, Mar. 2015.

[17] D. J. Pasadas, A. L. Ribeiro, H. G. Ramos, and T. J. Rocha, "Automatic parameter selection for Tikhonov regularization in ECT inverse problem," *Sens. Actuators A, Phys.*, vol. 246, pp. 73–80, Aug. 2016.

[18] M. A. Machado, K.-N. Antin, L. S. Rosado, P. Vilaça, and T. G. Santos, "Contactless high-speed eddy current inspection of unidirectional carbon fiber reinforced polymer," *Compos. B, Eng.*, vol. 168, pp. 226–235, Jul. 2019.

[19] D. M. Caetano *et al.*, "High-resolution nondestructive test probes based on magnetoresistive sensors," *IEEE Trans. Ind. Electron.*, vol. 66, no. 9, pp. 7326–7337, Sep. 2019.

[20] D. R. Desjardins, T. W. Krause, A. Tetervak, and L. Clapham, "Concerning the derivation of exact solutions to inductive circuit problems for eddy current testing," *NDT Int.*, vol. 68, pp. 128–135, Dec. 2014.

[21] J. O. Fava, L. Lanzani, and M. C. Ruch, "Multilayer planar rectangular coils for eddy current testing: Design considerations," *NDT E Int.*, vol. 42, no. 8, pp. 713–720, Dec. 2009.

[22] H. Zhou, B. Zhu, W. Hu, Z. Liu, and X. Gao, "Modelling and practical implementation of 2-coil wireless power transfer systems," *J. Electr. Comput. Eng.*, vol. 2014, pp. 1–8, Sep. 2014.

[23] D. I. Ona, G. Y. Tian, R. Sutthaweekul, and S. M. Naqvi, "Design and optimisation of mutual inductance based pulsed eddy current probe," *Measurement*, vol. 144, pp. 402–409, Oct. 2019.

[24] L. Xie, B. Gao, G. Y. Tian, J. Tan, B. Feng, and Y. Yin, "Coupling pulse eddy current sensor for deeper defects NDT," *Sens. Actuators A, Phys.*, vol. 293, pp. 189–199, Jul. 2019.

[25] D. I. Ona *et al.*, "Investigation of signal conditioning for Tx-Rx PEC probe at high lift-off using a modified Maxwell's bridge," *IEEE Sensors J.*, vol. 20, no. 5, pp. 2560–2569, Mar. 2019.

[26] Y. Cheng and Y. Shu, "A new analytical calculation of the mutual inductance of the coaxial spiral rectangular coils," *IEEE Trans. Magn.*, vol. 50, no. 4, pp. 1–6, Apr. 2014.

[27] C. Yang, B. Gao, Q. Ma, L. Xie, G. Y. Tian, and Y. Yin, "Multi-layer magnetic focusing sensor structure for pulsed remote field eddy current," *IEEE Sensors J.*, vol. 19, no. 7, pp. 2490–2499, Apr. 2019.

[28] L. Wei, C. Guoming, L. Wenyan, L. Zhun, and L. Feng, "Analysis of the inducing frequency of a U-shaped ACFM system," *NDT E Int.*, vol. 44, no. 3, pp. 324–328, May 2011.

[29] K. Chen, B. Gao, G. Y. Tian, Y. Yang, C. Yang, and Q. Ma, "Differential coupling double-layer coil for eddy current testing with high lift-off," *IEEE Sensors J.*, vol. 21, no. 16, pp. 18146–18155, Aug. 2021.

Yupei Yang received the B.Sc. degree from the School of Automation Engineering, University of Electronic Science and Technology of China, Chengdu, China, in 2019, where he is currently pursuing the M.Sc. degree in nondestructive testing using the eddy current technique.

His research interests include eddy current testing and wireless energy transfer.

Bin Gao (Senior Member, IEEE) received the B.Sc. degree in communications and signal processing from Southwest Jiaotong University, Chengdu, China, in 2005, and the M.Sc. (Hons.) degree in communications and signal processing and the Ph.D. degree from Newcastle University, Newcastle upon Tyne, U.K., in 2007 and 2011, respectively.

He worked as a Research Associate at Newcastle University from 2011 to 2013 on wearable acoustic sensor technology. He is currently a Professor with the School of Automation Engineering, University of Electronic Science and Technology of China (UESTC), Chengdu, China. He has coordinated several research projects from the National Natural Science Foundation of China. His research interests include electromagnetic and thermography sensing, machine learning, and nondestructive testing and evaluation, and he actively publishes in these areas.

Dr. Gao is also a very active reviewer of many international journals and long-standing conferences. His personal website is http://faculty.uestc.edu.cn/gaobin/zh_CN/lwcg/153392/list/index.htm.

Dong Liu (Member, IEEE) received the B.Sc. degree from the College of Physics, Sichuan University, Chengdu, China, in 2004, and the M.Sc. and Ph.D. degrees in control science and engineering from the University of Electronic Science and Technology of China, Chengdu, in 2010 and 2017, respectively.

He is currently a Research Associate with the School of Automation Engineering, University of Electronic Science and Technology of China. His research interests include crystal oscillators, piezoelectric sensors, and eddy current sensors.

Qiuping Ma received the B.Sc. degree in electronic information engineering from Sichuan Normal University, Chengdu, China, in 2017. She is currently pursuing the M.Sc. and Ph.D. degrees in nondestructive testing using eddy current technique with the University of Electronic Science and Technology of China, Chengdu.

Her research interests focus on eddy current testing including near-remote filed eddy current testing and eddy current array.

Haoran Li received the B.Sc. degree in electrical engineering and automation and the M.Sc. degree in control science and engineering from the Southwest University of Science and Technology, Mianyang, China, in 2015 and 2018, respectively. He is currently pursuing the Ph.D. degree with the University of Electronic Science and Technology of China, Chengdu, China.

His research mainly focuses on eddy current testing and thermography, as well as instrumentation manufacturing.

Wai Lok Woo (Senior Member, IEEE) received the B.Eng. degree in electrical and electronics engineering and the M.Sc. and Ph.D. degrees in statistical machine learning from Newcastle University, Newcastle upon Tyne, U.K., in 1993, 1995, and 1998, respectively.

He was the Director of Research of the Newcastle Research and Innovation Institute and the Director of Operations of Newcastle University. He is currently a Professor of Machine Learning with Northumbria University, Newcastle upon Tyne. His research interests include mathematical theory and algorithms for data science and analytics, artificial intelligence, machine learning, data mining, latent component analysis, multidimensional signals, and image processing. He has published more than 400 papers on these topics in various journals and international conference proceedings.

Dr. Woo is also a member of the Institution of Engineering and Technology. He was a recipient of the IEE Prize and the British Commonwealth Scholarship. He also serves as an Associate Editor for several international signal processing journals, including *IET Signal Processing*, the *Journal of Computers*, and the *Journal of Electrical and Computer Engineering*.

Gaige Ru received the M.Sc. degree in control science and engineering from Anhui Polytechnic University, Wuhu, China, in 2019. He is currently pursuing the Ph.D. degree with the University of Electronic Science and Technology of China, Chengdu, China.

His research mainly focuses on eddy current testing and magnetic flux leakage testing and instrumentation manufacturing. His research interests include smart sensors and system design for pipeline inspection.